Electrospun Zn$_{1-x}$Mn$_x$Fe$_2$O$_4$ Nanofibers As Anodes for Lithium-Ion Batteries and the Impact of Mixed Transition Metallic Oxides on Battery Performance

Pei Fen Teh,[†] Stevin Snellius Pramana,[†,‡] Yogesh Sharma,[§] Yah Wen Ko,[†] and Srinivasan Madhavi*[,†,⊥]

[†]School of Materials Science and Engineering and [‡]Facility for Analysis, Characterization Testing and Simulation, Nanyang Technological University, 50 Nanyang Avenue, Singapore

Nanyang Technological University, 50 Nanyang Avenue, Singapore

[§]Department of Applied Science and Engineering, Indian Institute of Technology Roorkee, Saharanpur Campus-247001, India

[⊥]Energy Research Institute @ NTU (ERIAN), Nanyang Technological University, CleanTech One, Singapore

Ⓢ *Supporting Information*

ABSTRACT: The structural and electrochemical properties of the mixed transition metallic oxides Zn$_{1-x}$Mn$_x$Fe$_2$O$_4$ nanofibers, which crystallize in a cubic spinel AFe$_2$O$_4$ structure, are investigated systematically with a gradual substitution of Zn by Mn. The crystal structural information studied by X-ray diffraction (XRD) depicts the formation of single phase spinel structure, while electron-dispersive X-ray spectroscopy (EDS) reveals the stoichiometric ratio between Zn and Mn. ZnFe$_2$O$_4$ exhibits a good capacity of ∼532 mAh g^{-1} at 50th cycle through the interbeneficial conversion reaction and alloy−dealloy mechanism, with a first discharge working voltage of ∼0.83 V. Subsequently, the characteristic redox potential of each spinel is gradually reduced with the replacement of Mn. Furthermore, Zn$_{0.3}$Mn$_{0.7}$Fe$_2$O$_4$ demonstrates the highest capacity of ∼612 mA h g^{-1} at 50th cycle among the solid solution series. Ex situ characterization by high-resolution transmission electron microscope (TEM) and electron energy loss spectroscopy (EELS) is conducted to study the participation of Mn in the battery performance. This report represents an example of how the electrochemical performance could be flexibly adjusted by tuning the ratio of transition metals within the spinel.

KEYWORDS: *electrospinning, transition metal oxides, nanofibers, ferrites, counterions, spinels*
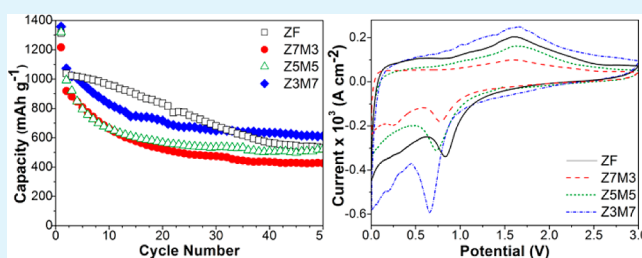
INTRODUCTION

Energy storage devices with renewable energy sources are anticipated as solution for depleting fossil fuels and various environmental issues.[1,2] Among various electrochemical energy storage solutions (such as nickel−metal-hydride batteries (NiMH) and lead-acid batteries),[3] lithium-ion battery (LIB) is anticipated as the most promising rechargeable power sources; for instance, it is successfully utilized in low power consumer's portable electronic appliances, because of its light weight, better specific energy density, and cycle durability.[4,5] However, current state-of-the-art LIBs cannot meet the high power/energy density and safety requirements for high-end applications including electric vehicles (EVs).[6] Hence, alternative high-energy-density LIB cathode/anode materials are required.[7]

Commercial LIB available in the consumer market contains lithium cobalt oxides (LiCoO$_2$) as cathode and graphite as anode. Because of the limited development of cathode based on their low theoretical capacity, a better anode is necessary in order to improve the overall performance of LIB. Amo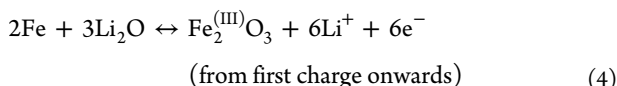ng various types of anodes, tr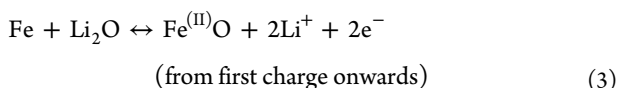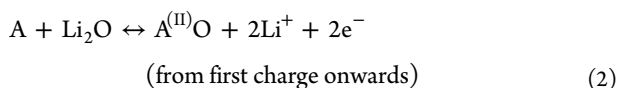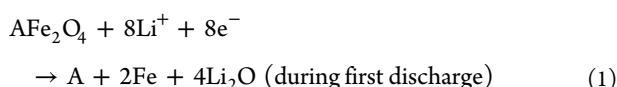ansition metal oxides (TMOs) have received considerable attention, as it can achieve high capacity in the range of ∼400−1000 mA h g^{-1},[8] which is higher than the theoretical capacity of commercially used graphite LIB anode (theoretical capacity = 372 mA h g^{-1}).[9] Co$_3$O$_4$[10−12] and Fe$_2$O$_3$[13−15] were widely investigated as anodes because they exhibit good lithium storage behavior, despite their high working voltages of ∼2.1 V versus Li$^+$/Li.[15,16] To reduce the working voltages, Zn has been substituted into Co$_3$O$_4$ and Fe$_2$O$_3$ to construct a ternary ZnCo$_2$O$_4$[17] and ZnFe$_2$O$_4$[18−20] spinels, with lower working voltages of ∼1.9 and ∼1.5 V, respectively. Although these preliminary studies show the competitive advantage of TMOs containing more than one transition metal as compared to their binary oxides,[17,20−22] extensive research studies on such TMO anodes with multiple transition metal are warranted.[8,17] AFe$_2$O$_4$ series (A$^{(II)}$ = Zn,[18−20] Mn,[23] Cu,[24,25] Ni,[25−27] etc.) have received greater attention than ACo$_2$O$_4$ series because of toxicity and cost of

cobalt.[28] Their storage mechanism toward lithium ions can be summarized as below

$$AFe_2O_4 + 8Li^+ + 8e^-$$

$$\rightarrow A + 2Fe + 4Li_2O \text{ (during first discharge)} \quad (1)$$

$$A + Li_2O \leftrightarrow A^{(II)}O + 2Li^+ + 2e^-$$

$$\text{(from first charge onwards)} \quad (2)$$

$$Fe + Li_2O \leftrightarrow Fe^{(II)}O + 2Li^+ + 2e^-$$

$$\text{(from first charge onwards)} \quad (3)$$

$$2Fe + 3Li_2O \leftrightarrow Fe_2^{(III)}O_3 + 6Li^+ + 6e^-$$

$$\text{(from first charge onwards)} \quad (4)$$

In general, 8 mols of lithium ions are taken by AFe_2O_4 at first discharge (eq 1), however this step is not reversible as the amorphization of AFe_2O_4 spinel takes place after first cycle,[18,20,29] forming $A/Fe/Li_2O$ nanocomposite, in which 2–5 nm of metallic nanograins are uniformly embedded in an amorphous Li_2O matrix. Equations 2–4 show the reversible lithium insertion/extraction behavior of AFe_2O_4 anodes from first charge cycle onward. A maximum of 8 mols of lithium ions can be reversibly released theoretically, by assuming A and Fe are fully oxidized to divalent and trivalent ions, respectively (eq 4). Nevertheless, incomplete reoxidation of Fe ions was observed in most of the previous publication, instead a mixture phase of $Fe^{(II)}O$ and $Fe_2^{(III)}O_3$ were found, leading to irreversible capacity.[18-20] Equations 3 and 4 are therefore reported to be coexistent at the subsequent cycling.

Following the identical reaction mechanism in eqs 1–4, nanocrystalline $CoFe_2O_4$, $NiFe_2O_4$, $ZnFe_2O_4$ and $CuFe_2O_4$ thin film studied by NuLi et al.[25] showed working voltage/capacity retention (at 100th cycles) of 1.7 V/365 mA h g^{-1}, 1.7 V/355 mA h g^{-1}, 1.6 V/432 mA h g^{-1}, and 1 V/340 mA h g^{-1}, respectively. From this, it can be seen that counterions tuning in AFe_2O_4 affects the working voltage and specific capacity.[22] It is also interesting to note that environmental friendly $ZnFe_2O_4$ generates better capacity as compared to other ferrites because lithium ions form an alloy with Zn reversibly, whereas Fe and Zn react with Li_2O to absorb/release lithium ions during lithiation/delithiation. Besides, intercalation of lithium ion into the $ZnFe_2O_4$ spinel was also observed at first discharge; however, it is not reversible as the amorphization of TMOs takes place during the first cycle.[18,20,29] Over the years, battery performance of $ZnFe_2O_4$ has been gradually enhanced by improving the preparation technology to form nanostructures.[18-20,29] The electrospinning method is a promising candidate for preparing anode nanomaterials because of the evident advantages, including being economic, scalable, and a simple technique.[30,31]

Our previous paper has shown the beneficial effect of one-dimensional electronic wiring for electrospun $ZnFe_2O_4$ nanofiber anode.[20] In this study, we further investigate the electrochemical impact of systematic replacement of Zn by Mn resulting in $Zn_{1-x}Mn_xFe_2O_4$ nanofibers. MnO is chosen to substitute ZnO as it has a lower working voltage of ~1.2 V[32] than $ZnFe_2O_4$, and MnO thin film[33] shows a higher reversible capacity of 650 mA h g^{-1} to compensate the low capacity of ZnO (~400 mA h g^{-1}), which is caused by low electronic conductivity and the large volume change in ZnO particles

during the cycling.[34] Thus, $Zn_{1-x}Mn_xFe_2O_4$ is predicted to possess higher capacity and lower working voltage as Mn content increases, while retaining the high cycleability of the $ZnFe_2O_4$.

■ EXPERIMENTAL SECTION

Detailed experimental procedure of $ZnFe_2O_4$ nanofibers by electrospinning has been reported elsewhere.[20] To obtain $Zn_{1-x}Mn_xFe_2O_4$ nanofibers ($0 \leq x \leq 1$), appropriate amount of $Zn(CH_3COO)_2 \cdot 2H_2O$ (Sigma Aldrich) was replaced by $Mn(CH_3COO)_2 \cdot 4H_2O$ (Sigma Aldrich) to mix with $Fe(NO_3)_3 \cdot 9H_2O$ (Sigma Aldrich) when preparing the electrospinning precursor solution. On the basis of the stoichiometric ratio, the samples were labeled as ZF ($x = 0$), Z7M3 ($x = 0.3$), Z5M5 ($x = 0.5$), Z3M7 ($x = 0.7$), and MF ($x = 1$) accordingly. To remove the poly(vinylpyrolidone) (PVP; Fluka) backbone and promote the oxide crystallization, we sintered as-spun ZF, Z7M3, Z5M5, and Z3M7 nanofibers at 450 °C, whereas fully replaced as-spun MF was sintered at 400 °C.

The morphology of the samples was examined by field-emission scanning electron microscope (FESEM, JEOL 7600F). The elemental compositions of the samples were analyzed by energy-dispersive X-ray spectroscopy (EDS) equipped to FESEM. The structural information was characterized by powder X-ray diffraction (Bruker D8 Advance, Cu Kα radiation, λ = 1.54 Å) with a step size of 0.05° over 15–80°. Rietveld refinement was performed using fundamental parameters peak shape profile[35] implemented in TOPAS.[36] A five-coefficient Chebychev polynomial background, a zero error, unit cell parameters, scale factor and crystallite size were sequentially refined. Thermogravimetric analysis (TGA) was performed using TA Instrument Q500 to monitor the thermal decomposition behavior of PVP by heating them from room temperature (r. t.) to 650 °C under air at a heating rate of 10 °C min^{-1}.

The electrochemical performances of $Zn_{1-x}Mn_xFe_2O_4$ nanofibers were examined in 2016-coin cell. The electrodes were prepared by mixing 60 wt % active materials, 20 wt % binder (Kynar), and 20 wt % Super P (Timcal) in solvent, N-methyl-pyrrolidinone (NMP, Sigma Aldrich) to form a homogeneous slurry. The slurry was coated on etched copper foil by doctor blade technique (thickness ~25 μm) and dried at 80 °C in vacuum oven for 12 h. Subsequently, the coating was pressed between twin rollers to improve the adhesion between copper foil and active materials. The electrodes were cut into circular disks with the diameter of 16 mm, and assembled in an argon filled glovebox (MBraun, Germany) with oxygen and water content less than 1 ppm. Lithium metal was served as a counter electrode, Celgard 2400 as the separator and 1 M solution of LiPF$_6$ dissolved in ethylene carbonate/diethylene carbonate (EC:DEC = 1:1 by volume, Charslton Technologies Pte. Ltd.) was used as electrolyte.

The lithium storage properties of $Zn_{1-x}Mn_xFe_2O_4$ nanofibers were examined by galvanostatic cycling (Multichannel Battery Tester, Neware Technology Limited) and cyclic voltammetry (CV, Solartron 1470E) measurements. The coin cells were galvanostatically discharged and charged in the voltage window of 0.005 - 3.0 V at room temperature with current density of 60 mA g^{-1}. CV testing was studied in the similar voltage range at a constant scanning rate of either 0.05 mV s^{-1} (first cycle) or 0.1 mV s^{-1} (fiftieth cycle). In order to understand the structural variation after the galvanostatic cycling, ex situ material characterization was conducted by high resolution transmission electron microscope (TEM), collected using JEOL 2100F microscope operated at 200 kV and fitted with a low-background Gatan double tilt holder. Electrode active material was peeled off from the current collector and rinsed with DEC in glovebox. It was ground into finer particles and ultrasonicated until homogeneous solution was achieved before dipping onto the TEM grids. EDS analysis was also conducted (equipped to TEM JEOL-2100F) on a respective region to confirm that the observation is on the active material, instead of Super P before collecting the selected area electron diffraction patterns (SAED) and electron energy loss spectra (EELS) results. The electron energy loss spectra (EELS) were obtained with a Gatan Imaging Filter (GIF) Quantum Spectrometer

with an energy resolution of ~1.2 eV using a collection half angle of β = 4 mrad, and spectra were collected with an energy dispersion of 0.25 eV per channel under STEM mode.

■ RESULTS AND DISCUSSION

Materials Characterization of Electrospun $Zn_{1-x}Mn_xFe_2O_4$ Nanofibers. Figure 1 illustrates the morphol-

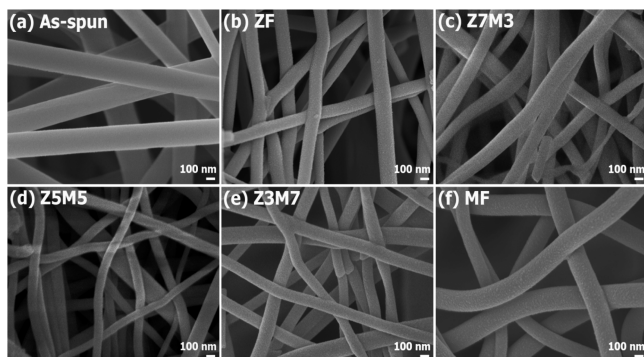**Figure 1.** FESEM images of (a) as-spun $Zn_{1-x}Mn_xFe_2O_4$ nanofibers, sintered (b) ZF, (c) Z7M3, (d) Z5M5, (e) Z3M7, and (f) MF nanofibers.

ogy of as-spun and sintered $Zn_{1-x}Mn_xFe_2O_4$ nanofibers. The as-spun nanofibers fall into the range of 200−280 nm in diameter (Figure 1a), while ZF ($x = 0$), Z7M3 ($x = 0.3$), Z5M5 ($x = 0.5$), and Z3M7 ($x = 0.3$) shrunk obviously to around 140−200 nm after the heat treatment at 450 °C (Figure 1b−e). This finding is analogous to our previous study,[20] which states that the sintering process at 450 °C caused the removal of PVP, which in turn decreased the diameter size of the nanofibers. MF ($x = 1$) (Figure 1f) has a larger diameter range of ~150−220 nm as it experienced a lower sintering temperature (400 °C) to preserve their crystal structure. Overall, all sintered samples show a continuous framework of nanofibers with open pores, smooth surface and uniform diameter despite Mn substitution. The electrospun nanofibers exhibit no traces of agglomeration and successfully form a connective framework that may be favorable for lithium-ion kinetics.

XRD patterns (Figure 2a) represent the structural information of $Zn_{1-x}Mn_xFe_2O_4$ nanofibers obtained after the sintering process. After Rietveld refinement, the XRD result of ZF ensures the formation of a single phase cubic spinel structure ($Fd\bar{3}m$) with good agreement with ICSD no. 162646. The peaks at $2\theta = 18.1°$, 30.0, 35.1, 36.7, 42.8, 53.1, 56.7, 62.1, 70.5, and 73.5° correspond to Miller indices (hkl) of (111), (220), (311), (222), (400), (422), (333/511), (440), (620), and (533), resembling XRD patterns are also observed in Z7M3, Z5M5 and Z3M7. Besides, similar synthesis condition was applied on MF; however, nanofibers sintered at 450 °C form $MnFe_2O_4$ spinel phase with a high amount of Fe_2O_3 as impurities. If the sintering temperature was raised to 500 °C, $MnFe_2O_4$ totally disintegrated into a combination of Mn_2O_3 and Fe_2O_3 (see the Supporting Information, Figure S1). To prevent the decomposition of spinel into binary oxides, as-spun MF nanofibers were heated at only 400 °C, but it has led to a XRD pattern with very low signal-to-noise ratio as 400 °C is lower than PVP decomposition temperature (440 °C, see the Supporting Information, Figure S2). To sum up, when the Zn is fully replaced by Mn, i.e., MF ($x = 1$), we could not produce a single phase spinel either using the maximum sintering
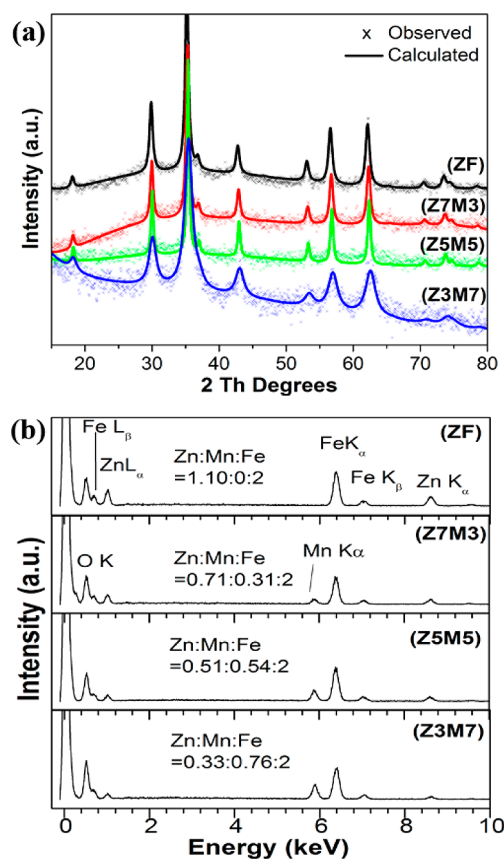
Figure 2. (a) XRD Rietveld refined patterns with the observed data (b) EDS analysis of sintered ZF, Z7M3, Z5M5, and Z3M7 nanofibers.

temperature of 400, 450, or 500 °C, multiple phases were observed. Hence, MF was excluded from the systematic comparison as it does not form a pure phase spinel. It is well-known that the cation distribution has a significant impact on physical properties.[37−39] A and B sites were refined sequentially to be occupied by Zn, Mn, or Fe by Rietveld method (refer to the Supporting Information, Table S1). However, because of the fact that the number of electrons of these three cations are very similar, the scattering factors may be indistinguishable and therefore the values presented in this report might not be precise since the XRD peaks are broadened based on the presence of numerous nanocrystals which forming the nanofibers. Thus, further work using extended X-ray absorption fine structure (EXAFS) and X-ray absorption near edge structure (XANES) are going to be performed in synchrotron facility to elucidate the possible coordination environment in each cation.

To quantify the ratio of Zn and Mn ions toward Fe ions, electron-dispersive X-ray spectroscopy (EDS) was conducted on sintered ZF, Z7M3, Z5M5, and Z3M7. We normalized the element ratio by taking Fe as 2 mols. The analysis shows a substantial decrement of Zn L_α and K_α peaks as the Mn replacement increases. On the contrary, the Mn K_α peak gets more and more intense, so all samples were successfully prepared on the basis of the presumed stoichiometric ratio and were applied as LIB anodes to understand the impact of Mn substitution on battery performance.

Battery Performance of Electrospun $Zn_{1-x}Mn_xFe_2O_4$ ($0 \leq x \leq 0.7$) Nanofibers as LIB Anodes. To understand the influence of Mn substitution in spinel structure on battery

performance, we recorded galvanostatic cycling of electrospun $Zn_{1-x}Mn_xFe_2O_4$ nanofibers at a current density of 60 mA g^{-1} in the potential window of 0.005 − 3.0 V (Figure 3a). ZF reacts
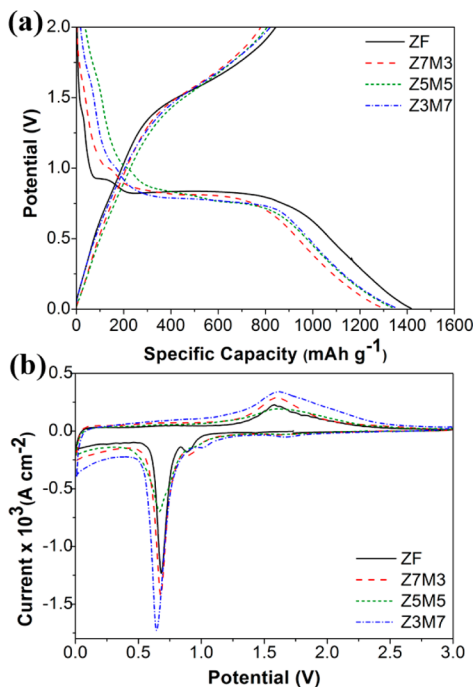

Figure 3. (a) First galvanostatic cycle (current density = 60 mA g^{-1}), and (b) first cycle of CV scan (scan rate = 0.05 mV s^{-1}) of ZF, Z7M3, Z5M5, and Z3M7 nanofibers.

with lithium ions in a similar mechanism as our previous publications,[18,20] in which a very short plateau is observed at ∼1.4 V, and another plateau is seen at ∼0.9 V due to the intercalation of lithium ions into the spinel layered structure. Similarly, these two short plateaus are noticed in Z7M3, Z5M5 and Z3M7. Subsequently, a long discharge plateau was observed at ∼0.83 V in the first discharge cycle of ZF (Figure 3a), which can be speculated as the working voltage when crystal destruction occurs due to the conversion reaction of $ZnFe_2O_4$ into Li_2O, Zn, and Fe.[18,20,29] This prediction is coherent with Sharma et al.[18] as the destruction of crystal happens at ∼0.8 V. Likewise, the first discharge destruction plateau was also observed in other samples, while this characteristic plateau is slightly lower in Z7M3 (∼0.81 V), Z5M5 (∼0.8 V), and Z3M7 (∼0.76 V).

Cyclic voltammetry (CV) was conducted between 0.005 and 3.0 V at 0.05 mV s^{-1} (Figure 3b) to identify the average working voltage of electrospun $Zn_{1-x}Mn_xFe_2O_4$ nanofibers. Reduction peaks of $ZnFe_2O_4$ demonstrate same information as their galvanostatic cycling, i.e., two irreversible shallow peaks at ∼1.66 V and ∼0.92 V indicate the intercalation of lithium ions. In general, these two reduction peaks were also noted in another three samples. There is no corresponding oxidation peaks found in reverse oxidation scan, as the spinel structure is thoroughly amorphized after first discharge. Similar decrement of conversion reaction working voltages were also recorded in the CV, the conversion reaction peak of ZF was found to be ∼0.69 V, whereas a lower peak of ∼0.68, 0.67, and ∼0.64 V was presented by Z7M3, Z5M5 and Z3M7. Hence, Mn substitution in electrospun $Zn_{1-x}Mn_xFe_2O_4$ nanofibers successfully brought down the working voltage. This is analogue to the report by Li

et al.,[32,40] in which working voltage of oxides in eq 2 can be speculated by Nernst equation, as below

$$\Delta G^0 = \Delta G^0(Li_2O) - \Delta G^0(AO) = -nEF \quad (5)$$

Here AO represents TMOs (either MnO or ZnO), n corresponds to the number of the charge transferred during the reaction per mole of AO, E refers to the electromotive force (emf) or working voltage mentioned in this report, F is the Faraday constant. Since MnO has lower Gibbs free energy of formation ($\Delta G^0 = -363$ kJ mol^{-1}) than ZnO ($\Delta G^0 = -320$ kJ mol^{-1}), so working voltage slightly decreases when the Mn ratio is higher.

From the perspective of lithium-ion storage capability, Figure 3a illustrates the lithium insertion/extraction performance exhibited by electrospun $Zn_{1-x}Mn_xFe_2O_4$ nanofibers. The capacities are comparable at the initial cycling. Total first discharge/charge capacities achieved by ZF, Z7M3, Z5M5 and Z3M7 are 1417/1025 mA h g^{-1}, 1302/948 mA h g^{-1}, 1344/972 mA h g^{-1}, 1358/1015 mA h g^{-1}, respectively. The correlating Coulombic efficiencies at first cycle fall in the range of 72−75%. Hence, a slight variation of the capacity values can be attributed by the different degree of electrolyte decomposition or solid electrolyte interphase (SEI) formation on electrodes.[1,15,41] To understand the impact of replacing Zn by Mn, cycling performance is shown in Figure 4a after 50 discharge/charge
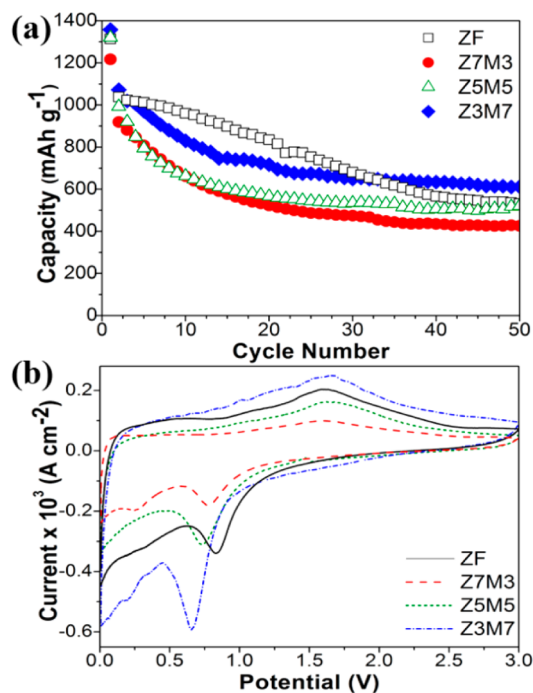

Figure 4. (a) Extended cycling data of electrospun $Zn_{1-x}Mn_xFe_2O_4$ nanofibers and (b) their corresponding CV scans after 50th cycle at scan rate of 0.1 mV s^{-1}.

cycle at 60 mA g^{-1}. The observed capacity depleted slowly for the first few cycles and eventually reached a stable capacity up to 50 cycles. Reversible capacity is one of the key factors for selecting anode material in LIBs, so increasing composition of Mn in $Zn_{1-x}Mn_xFe_2O_4$ nanofibers has shown success in effectively enhancing the reversible capacity in the anodes. After 50 cycles, Z3M7 demonstrates the highest reversible capacity of ∼612 mA h g^{-1} as compared to Z5M5 with capacity of ∼521 mA h g^{-1}, Z7M3 of ∼426 mA h g^{-1} and ZF with

capacity of ~532 mA h g^{-1}. The reversible capacity of Z3M7 retained is almost two times higher than the capacity of 372 mAh g^{-1} given by commercial graphite.[42] Figure 4b has shown consecutive CV scan after 50 cycles, all samples have exhibited identical curves in shape. It is worth noting that the discharge working voltage is consistently lower if the Mn composition is higher. The systematic study of solid solution in AFe_2O_4 is reported for the first time, and it has verified the possibility to adjust the working voltage by varying the counterions.[43] The discharge voltage of ZF is ~0.84 V, Z7M3 at ~0.78 V, and Z5M5 at ~0.73 V, whereas Z3M7 depicts the lowest discharge voltage at ~0.66 V.

Participation of Mn in Electrospun $Zn_{1-x}Mn_xFe_2O_4$ (0 ≤ x ≤ 0.7) nanofibers. There were many reports using ex situ TEM to verify the phase formation within electrode after prolonged cycling.[43−45] As previously reported,[20] $ZnFe_2O_4$ can reversibly absorb/release lithium ions by interbeneficial conversion reaction and alloy-dealloy mechanism,[18,20] TEM has shown some ambiguous speculation of the formation of FeO, ZnO, Fe_2O_3 or LiZn after 50th cycle. Therefore, ZF has exhibited a good capacity of ~532 mA h g^{-1} at 50th cycle (Figure 4a). In this report, Z7M3 has a poorer capacity despite of their lower working voltage than ZF, but Z5M5 and Z3M7 have achieved a better cycling stability, so it is important to determine the reaction mechanism of Mn within $Zn_{1-x}Mn_xFe_2O_4$ nanofibers. Similar ex situ TEM study has been conducted on Z7M3 (Figure 5a), diffuse set of concentric

Table 1. d-Spacings and Possible Miller Indices of the SAED Pattern of ex Situ Z7M3 and Z3M7 in Figure 5a,b

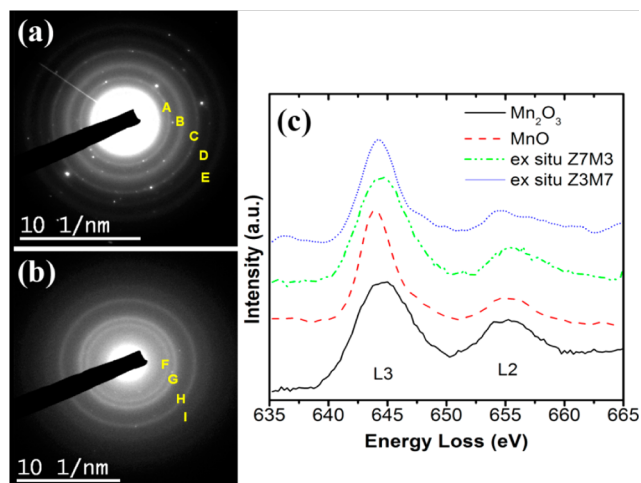| label	d-spacing experimental value (Å)	phase	Miller index	d-spacing reported value (Å)	ref
A	2.74	Fe_2O_3	(104)	2.70	ICSD #173651
		Mn_2O_3	(222)	2.72	ICSD #180891
B	2.18	FeO	(200)	2.16	ICSD #633038
C	1.71	Fe_2O_3	(116)	1.70	ICSD #173651
		Mn_2O_3	(440)	1.66	ICSD #180891
D	1.44	LiZn	(331)	1.43	ICSD #104792
E	1.25	FeO	(222)	1.24	ICSD #633038
F	2.52	MnO	(111)	2.57	ICSD #643195
		Mn_2O_3	(301)	2.55	ICSD #180891
G	2.20	FeO	(200)	2.15	ICSD #633038
H	1.55	FeO	(220)	1.52	ICSD #633038
I	1.26	FeO	(222)	1.24	ICSD #633038

Figure 5. Ex situ SAED patterns of (a) Z7M3 and (b) Z3M7 nanofibers display a diffuse set of concentric rings, indicating the nanocrystalline nature of the charged electrode after 50th cycle. (c) Mn $L_{2,3}$ edges of ex situ Z7M3 and Z3M7 collected by ELNES; MnO and Mn_2O_3 are taken as references.

rings indicates the charged Z7M3 electrode consists of nanocrystalline regions dispersed in amorphous matrix. The d-spacings and their respective Miller indices were retrieved from SAED data and summarized in Table 1, a mixed phase of LiZn, FeO, Fe_2O_3 and Mn_2O_3 coexists in charged state, whereas ZnO is not observed, possibly because of the poor cycleability of ZnO anodes that has been widely reported.[34,46,47] It is unusual to discover the formation of Mn_2O_3, instead of MnO, as there is no report regarding an increase of oxidation state than its initial state after extended cycling. Subsequently, the presence of Mn^{3+} after reversible cycling has again been ambiguously observed in ex situ SAED of Z3M7 electrode
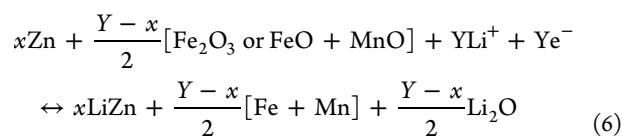
(Figure 5b). It is worth noting that the reaction mechanism of TMO is difficult to accurately characterize by TEM because of the fine-grained and heterogeneous nature of the electrode. Because of it, electron-energy loss near-edge structure (ELNES) spectrum was collected to determine the valence state of Mn 3d (Figure 5c), in order to gain a more reliable analysis than ex situ TEM.

Representative EELS spectra Mn L-edge from commercial MnO and Mn_2O_3 are recorded in Figure 5c as references to quantitatively calibrate the peak energies. Two broad Mn L_2 and L_3 peak onsets were observed at ~640 and ~651 eV respectively, which is same as the interpretation by Garvie et al.[48] The L-edge of Mn^{2+} and Mn^{3+} are characterized by the L_3/L_2 white-line ratio resulting from the ratio of electronic transition from the spin−orbit levels $2p_{3/2}$ and $2p_{1/2}$ to unoccupied 3d states, respectively. Hence, the white-line ratio has a strong relation with the spin state of a transition metal, and thus it can quantitatively calculate chemical state of an element.[49,50] In this report, the L_3/L_2 white-line ratios were obtained by first removing the background using a power law fitting, whereas plural scattering was considered by Fourier ratio deconvolution with the zero loss regions. For a consistent calculation, energy width of 6 eV centered on the L peak maxima was chosen as the integral window for all samples, with the purpose to minimize the discrepancy (refer to the Supporting Information, Figure S3). The results are summarized in Table 2. It can be summarized that MnO forms at the charged state of Z7M3 and Z3M7, instead of Mn_2O_3. This finding obeys the reported reaction mechanism in conversion reaction of Mn-based TMOs,[51] and hence the increase of valence state than its initial state is not physically possible in conversion reaction. Therefore, EELS is a better characterization tool than TEM in ex situ study, especially when the valence state of charged/discharged electrode is the main interest.

Table 2. Mn $L_{2,3}$ ELNES Data As Measured by EELS Analysis (Figure 5c)

sample	Mn intensity ratio (L_3/L_2)	reported Mn intensity ratio (L_3/L_2)	ref
Mn_2O_3	2.62	2.50	49
		2.40	50
MnO	4.00	3.98	49
		3.90	50
Z7M3	3.91		
Z3M7	3.99		

On the basis of the observation by ex situ TEM and EELS studies, reversible capacities given by Z7M3, Z5M5, and Z3M7 at 50th cycle, i.e., ~3.8, ~4.6, and ~5.3 mols of lithium ions per formula unit can be correlated to the reaction stated in eq 6, and Y represents the number of lithium ions transferred during the reaction, respectively. MnO has exhibited greater reversibility and a lower discharge voltage than ZnO, so better capacity retention was achieved when the amount of Mn increases within the spinel. Owing to it, it is possible to alter the performance of LIB spinel-anodes by selectively tuning the ratio of mixed TMOs.

$$xZn + \frac{Y-x}{2}[Fe_2O_3 \text{ or } FeO + MnO] + YLi^+ + Ye^-$$

$$\leftrightarrow xLiZn + \frac{Y-x}{2}[Fe + Mn] + \frac{Y-x}{2}Li_2O \qquad (6)$$

CONCLUSION

Synthesis and systematic electrochemical study of electrospun $Zn_{1-x}Mn_xFe_2O_4$ nanofibers were demonstrated for the first time. One-dimensional nanofibers have successfully exhibit excellent battery properties, due to the presence of a connective framework, which is beneficial for lithium-ion kinetics. A lower discharge voltage and better cycleability were achieved by substituting the Zn with Mn in the spinel anodes, hence it provides an insight about the possibility to change the battery performance by altering the molar ratio within a mixed transition metallic oxides. Tuning of working voltage of anode is crucial in deciding the overall voltage output of LIB. Ex situ characterization by TEM and EELS have witnessed the presence of Mn^{2+} in the charged electrode, and EELS is a better characterization tool for ex situ study in battery performance.

ASSOCIATED CONTENT

Ⓢ Supporting Information

XRD patterns of electrospun MF with impurities, TGA analysis of PVP, positions of integration windows in EELS analysis. This material is available free of charge via the Internet at http://pubs.acs.org/.

AUTHOR INFORMATION

Corresponding Author

*E-mail: madhavi@ntu.edu.sg.

Notes

The authors declare no competing financial interest.

ACKNOWLEDGMENTS

REFERENCES

(1) Liu, C.; Li, F.; Lai-Peng, M.; Cheng, H. M. *Adv. Mater.* **2010**, *22*.
(2) Li, H.; Wang, Z.; Chen, L.; Huang, X. *Adv. Mater.* **2009**, *21*, 4593−4607.
(3) Winter, M.; Brodd, R. J. *Chem. Rev.* **2004**, *104*, 4245−4269.
(4) Tarascon, J. M.; Armand, M. *Nature* **2001**, *414*, 359−367.
(5) Bruce, P. G.; Scrosati, B.; Tarascon, J. M. *Angew. Chem., Int. Ed.* **2008**, *47*, 2930−2946.
(6) Tarascon, J. M. *Philos. Trans. R. Soc. London, Ser. A* **2010**, *368*, 3227−3241.
(7) Manthiram, A.; Vadivel Murugan, A.; Sarkar, A.; Muraliganth, T. *Energy Environ. Sci.* **2008**, *1*, 621−638.
(8) Cabana, J.; Monconduit, L.; Larcher, D.; Palacín, M. R. *Adv. Mater.* **2010**, *22*, E170−E192.
(9) Tran, T. D.; Feikert, J. H.; Pekala, R. W.; Kinoshita, K. *J. Appl. Electrochem.* **1996**, *26*, 1161−1167.
(10) Guo, B.; Li, C.; Yuan, Z. Y. *J. Phys. Chem. C* **2010**, *114*, 12805−12817.
(11) Kang, Y.-M.; Song, M.-S.; Kim, J.-H.; Kim, H.-S.; Park, M.-S.; Lee, J.-Y.; Liu, H. K.; Dou, S. X. *Electrochim. Acta* **2005**, *50*, 3667−3673.
(12) Shaju, K. M.; Jiao, F.; Débart, A.; Bruce, P. G. *Phys. Chem. Chem. Phys.* **2007**, *9*, 1837−1842.
(13) Larcher, D.; Masquelier, C.; Bonnin, D.; Chabre, Y.; Masson, V.; Leriche, J. B.; Tarascon, J. M. *J. Electrochem. Soc.* **2003**, *150*, A133−A139.
(14) NuLi, Y.; Zeng, R.; Zhang, P.; Guo, Z.; Liu, H. *J. Power Sources* **2008**, *184*, 456−461.
(15) Reddy, M. V.; Yu, T.; Sow, C. H.; Shen, Z. X.; Lim, C. T.; Rao, G. V. S.; Chowdari, B. V. R. *Adv. Funct. Mater.* **2007**, *17*, 2792−2799.
(16) Badway, F.; Plitz, I.; Grugeon, S.; Laruelle, S.; Dollé, M.; Gozdz, A. S.; Tarascon, J. M. *Electrochem. Solid-State Lett.* **2002**, *5*, A115−A118.
(17) Sharma, Y.; Sharma, N.; Subba Rao, G. V.; Chowdari, B. V. R. *Adv. Funct. Mater.* **2007**, *17*, 2855−2861.
(18) Sharma, Y.; Sharma, N.; Rao, G. V. S.; Chowdari, B. V. R. *Electrochim. Acta* **2008**, *53*, 2380−2385.
(19) NuLi, Y. N.; Chu, Y. Q.; Qin, Q. Z. *J. Electrochem. Soc.* **2004**, *151*, A1077−A1083.
(20) Teh, P. F.; Sharma, Y.; Pramana, S. S.; Srinivasan, M. *J. Mater. Chem.* **2011**, *21*, 14999−15008.
(21) Teh, P. F.; Sharma, Y.; Ko, Y. W.; Pramana, S. S.; Srinivasan, M. *RSC Advances* **2013**, *3*, 2812−2821.
(22) Courtel, F. M.; Duncan, H.; Abu-Lebdeh, Y.; Davidson, I. J. *J. Mater. Chem.* **2011**, *21*, 10206−10218.
(23) Zhang, D.; Zhang, X.; Ni, X.; Song, J.; Zheng, H. *Chem. Phys. Lett.* **2006**, *426*, 120−123.
(24) Kalai Selvan, R.; Kalaiselvi, N.; Augustin, C. O.; Doh, C. H.; Sanjeeviraja, C. *J. Power Sources* **2006**, *157*, 522−527.
(25) NuLi, Y.-N.; Qin, Q.-Z. *J. Power Sources* **2005**, *142*, 292−297.
(26) Lavela, P.; Tirado, J. L. *J. Power Sources* **2007**, *172*, 379−387.
(27) Zhao, H.; Zheng, Z.; Wong, K. W.; Wang, S.; Huang, B.; Li, D. *Electrochem. Commun.* **2007**, *9*, 2606−2610.
(28) Lauwerys, R.; Lison, D. *Sci. Total Environ.* **1994**, *150*, 1−6.
(29) Guo, X.; Lu, X.; Fang, X.; Mao, Y.; Wang, Z.; Chen, L.; Xu, X.; Yang, H.; Liu, Y. *Electrochem. Commun.* **2010**, *12*, 847−850.
(30) MacIas, M.; Chacko, A.; Ferraris, J. P.; Balkus, K. J., Jr. *Microporous Mesoporous Mater.* **2005**, *86*, 1−13.
(31) Li, D.; Xia, Y. *Adv. Mater.* **2004**, *16*, 1151−1170.

5466

dx.doi.org/10.1021/am400497v | *ACS Appl. Mater. Interfaces* 2013, 5, 5461−5467

(32) Li, H.; Balaya, P.; Maier, J. *J. Electrochem. Soc.* **2004**, *151*, A1878−A1885.

(33) Yu, X. Q.; He, Y.; Sun, J. P.; Tang, K.; Li, H.; Chen, L. Q.; Huang, X. J. *Electrochem. Commun.* **2009**, *11*, 791−794.

(34) Wang, H.; Pan, Q.; Cheng, Y.; Zhao, J.; Yin, G. *Electrochim. Acta* **2009**, *54*, 2851−2855.

(35) Cheary, R. W.; Coelho, A. *J. Appl. Crystallogr.* **1992**, *25*, 109−121.

(36) *SAINT*, version 6.0; Bruker: Madison, WI, 2005.

(37) Yoon, S. J.; Lee, S. H.; Kim, K. H.; Ahn, K. S. *Mater. Chem. Phys.* **2002**, *73*, 330−334.

(38) Catti, M.; Freyria Fava, F.; Zicovich, C.; Dovesi, R. *Phys. Chem. Miner.* **1999**, *26*, 389−395.

(39) Lenaz, D.; Skogby, H.; Princivalle, F.; Hålenius, U. *Phys. Chem. Miner.* **2004**, *31*, 633−642.

(40) Zu, C. X.; Li, H. *Energy Environ. Sci.* **2011**, *4*, 2614−2624.

(41) Balaya, P. *Energy Environ. Sci.* **2008**, *1*, 645−654.

(42) Buqa, H.; Goers, D.; Holzapfel, M.; Spahr, M. E.; NovÃk, P. *J. Electrochem. Soc.* **2005**, *152*.

(43) Kim, H.; Seo, D. H.; Park, I.; Hong, J.; Park, K. Y.; Kang, K. *Chem. Mater.* **2012**, *24*, 720−725.

(44) Sharma, Y.; Sharma, N.; Subba Rao, G. V.; Chowdari, B. V. R. *Solid State Ionics* **2008**, *179*, 587−597.

(45) Sharma, Y.; Sharma, N.; Rao, G. V. S.; Chowdari, B. V. R. *Chem. Mater.* **2008**, *20*, 6829−6839.

(46) Liu, J.; Li, Y.; Ding, R.; Jiang, J.; Hu, Y.; Ji, X.; Chi, Q.; Zhu, Z.; Huang, X. *J. Phys. Chem. C* **2009**, *113*, 5336−5339.

(47) Li, C.; Yu, Z.; Fang, S.; Wang, H.; Gui, Y.; Xu, J.; Chen, R. *J. Alloys Compd.* **2009**, *475*, 718−722.

(48) Garvie, L. A. J.; Craven, A. J.; Brydson, R. *Am. Mineral.* **1994**, *79*, 411−425.

(49) Tan, H.; Verbeeck, J.; Abakumov, A.; Van Tendeloo, G. *Ultramicroscopy* **2012**, *116*, 24−33.

(50) Schmid, H. K.; Mader, W. *Micron* **2006**, *37*, 426−432.

(51) Lin, Z.; Ji, L.; Woodroof, M. D.; Zhang, X. *J. Power Sources* **2010**, *195*, 5025−5031.

5467

dx.doi.org/10.1021/am400497v | *ACS Appl. Mater. Interfaces* 2013, 5, 5461−5467